A simple and efficient model for orographic precipitation

Stefan Hergarten[1] and Jörg Robl[2]

[1]Institut für Geo- und Umweltnaturwissenschaften, Albert-Ludwigs-Universität Freiburg, Albertstr. 23B, 79104 Freiburg, Germany
[2]Department of Geography and Geology, University of Salzburg, 5020 Salzburg, Austria

Correspondence: Stefan Hergarten
(stefan.hergarten@geologie.uni-freiburg.de)

Abstract. The influence of climate on landform evolution has received great interest over the past decades. While many studies aim at determining erosion rates or parameters of erosion models, feedbacks between tectonics, climate and landform evolution have been discussed, but addressed quantitatively only in a few modeling studies. One of the problems in this field is that coupling a large-scale landform evolution model with a general circulation model would dramatically increase the theoretical and numerical complexity. Only a few simple models are available so far that allow a numerical efficient coupling between topography-controlled precipitation and erosion. This paper fills this gap by introducing a quite simple approach involving two vertically integrated moisture components (vapor and cloud water). The interaction between both components is linear and depends on altitude. This model structure is in principle the simplest approach that is able to predict both orographic precipitation at small scales and a large-scale decrease in precipitation over continental areas without introducing additional assumptions. Even in combination with transversal dispersion and height-dependent evapotranspiration, the model is of linear time complexity and increases the computing effort of efficient large-scale landform evolution models only moderately. Even simple numerical experiments applying such a coupled landform evolution model show the strong impact of spatial precipitation gradients on mountain range geometry including steepness and peak elevation, position of the principal drainage divide, and drainage network properties.

1 Introduction

The redistribution of moisture from the oceans towards continental domains governs the global erosion engine. Spatial variability in precipitation and hence in the availablility of water or ice as principal agents of erosion control the shape of individual landforms (e.g, Menking et al., 2013; Chen et al., 2019) or even the the geometry of entire mountain ranges (e.g., Ellis et al., 1999; Willett, 1999; Bonnet, 2009; Goren et al., 2014). However, feedbacks between topography, precipitation and erosion may even make it difficult to distinguish between cause and effect (Molnar and England, 1990).

Long-term fluvial erosion is a field where simple numerical models have been applied with great success for some decades. The simplest model in this context is often referred to as the stream-power incision model (SPIM) and is the key component of several models of long-term fluvial landform evolution (for an overview, see, e.g., Willgoose, 2005; Wobus et al., 2006). The SPIM considers rivers as linear elements (so without explicitly accounting for the width and the cross-sectional shape) and

25 predicts the erosion rate E as a function of the upstream catchment size A and the channel slope S in the form

$$E = KA^m S^n. \tag{1}$$

While the exponents m and n are assumed to be more or less universal, all site-specific influences on erosion are subsumed in a single lumped parameter K, called erodibility. The SPIM in its original form (Eq. 1) implements the concept of bedrock incision in the sense that all particles once detached from the bedrock are immediately excavated. The applicability of this

30 concept even to bedrock rivers in high mountain regions has been questioned (e.g., Turowski, 2012). However, considerable progress has been made concerning including sediment transport in the SPIM both theoretically and numerically (Davy and Lague, 2009; Yuan et al., 2019; Hergarten, 2020). Even extensions towards glacial erosion were recently proposed (Deal and Prasicek, 2021; Hergarten, 2021).

The SPIM and its derivates are well-suited for problems of tectonic geomorphology, e.g., varations in uplift rate or contrasts

35 in lithology. In turn, the occurence of the erodibility as a single, lumped parameter is a serious limitation concerning the influence of precipitation.

A framework for extending the SPIM towards a spatial variation in precipitation was already applied in several studies (e.g., Yanites and Ehlers, 2012; Goren et al., 2014; Garcia-Castellanos and Jiménez-Munt, 2015; Salles, 2016; Yuan et al., 2019). The idea is that erosion rates should rather depend on discharge than on catchment size, although the SPIM (Eq. 1) is typically

40 written in terms of catchment size for historical reasons. Let P be the effective precipitation for the moment, i.e., the part of the precipitation that contributes to discharge. If we assume that the actual erodibility K refers to a given uniform reference precipitation P_0 and thus to a reference discharge $q_0 = P_0 A$, the catchment size A can be replaced by $\frac{q_0}{P_0}$ in Eq. (1). It is then assumed that Eq. (1) holds for any discharge q if A is replaced by $\frac{q}{P_0}$. Since the equations become somewhat cumbersome if q is replaced by the integral of P over the upstream catchment, Hergarten (2021) defined

45 $$A_{\text{eq}} = \frac{q}{P_0} \tag{2}$$

as the catchment-size equivalent of the discharge. It defines the catchment size needed to generate the actual discharge q at the reference precipitation P_0. The advantage of using this terminology is that all relations in the context of erosion keep their simplicity, just with A_{eq} instead of A.

One might think of using scenarios of a general circulation model for computing precipitation. However, this would not

50 only require a high computing effort, but also introduce several additional degrees of freedom. In sum, there would be a huge imbalance between the complexity of the precipitation model and the simplicity of the erosion model. Preserving this simplicity requires simple models focusing on orographic effects on the relative precipitation $\frac{P}{P_0}$, which allows for computing A_{eq} (Eq. 2). The main challenge is finding a level of complexity that still provides new insights into landform evolution although the model is inevitably oversimplified from the point of view of meteorology.

55 On a fundamental level, even extremely simple approaches were used. Goren et al. (2014) distinguished between the windward side and the leeward side of a mountain belt just by the main drainage divide and assigned an increased relative precipitation to the windward region. This extremely simple model turned out to be sufficient for explaining a shift and an asymmetry in the drainage divide.

In turn, the models proposed by Roe et al. (2003), Smith and Barstad (2004), and Garcia-Castellanos (2007) use the concept
of vertically integrated water contents and the respective fluxes per unit width. Assuming steady-state conditions, precipitation
is derived from the negative divergence of the flux per unit width. All these models bring the topography into play by a
thermodynamic equilibrium that depends on height via temperature.

The earliest among these models (Roe et al., 2003), however, does not model any fluxes explicitly, but directly proposes
an equation for the divergence and thus for precipitation. The model predicts the rate of precipitation explicitly as a function
of local surface height and slope in wind direction. As the only non-local component of the model, a Gaussian smoothing
in upwind direction was used in order to reduce effects of surface roughness. Due to these properties, the model is able to
reproduce an increased precipitation at the windward side compared to the leeward side of a mountain belt, but fails to describe
the large-scale shadow in a plane behind the mountain range or the decrease in precipitation with increasing distance to the
ocean.

The two other models (Smith and Barstad, 2004; Garcia-Castellanos, 2007) consider spatially variable water contents and
the respective fluxes, where transport at a given wind velocity is assumed. The model proposed by Smith and Barstad (2004)
defines two components, interpreted as cloud water and hydrometeors. This model focuses on condensation and fallout at small
scales, while it cannot predict transport over long distances. It therefore requires a refilling from an additional reservoir and is,
similarly to the model of Roe et al. (2003), not able to predict large-scale precipitation patterns. In turn, the model of Garcia-
Castellanos (2007) describes the vertically integrated water content by a single variable. Using a quite ingenious approach for
describing deviations from equilibrium, it is able to capture the increase in precipitation with altitude as well the slow decrease
in precipitation with increasing distance from the ocean. In turn, it requires an artificial smoothing at small scales, similarly to
the model of Roe et al. (2003).

The goal of this paper is developing a model that captures both the direct response of precipitation to changes in topography
and large-scale precipitation patterns without the need for ad hoc assumptions such as an additional reservoir or smoothing.
Beyond this, the numerical complexity should be not much higher than in the existing models. In particular, the linear time
complexity (i.e., that the computing effort increases only linearly with the grid size) achieved by contemporary fluvial landform
evolution models (Hergarten and Neugebauer, 2001; Braun and Willett, 2013; Yuan et al., 2019; Hergarten, 2020) should be
preserved.

2 Model description

The model developed in the following is inspired by the concepts of Smith and Barstad (2004) and Garcia-Castellanos (2007).
Similarly to these models, we describe the distribution of water in the atmosphere in terms of vertically integrated water
contents measured in m, which can be interpreted as water column heights. Following the ideas of Smith and Barstad (2004),
we use two components, while the model of Garcia-Castellanos (2007) uses a single component and thus seems to be simpler
at first sight. However, we will see in Sect. 4.1 that the effort of using two components pays off.

2.1 The governing equations

Let u_v be the content of vapor and u_c be the content of cloud water, both vertically integrated and measured as the height of a water column. Following the concepts of Smith and Barstad (2004) and Garcia-Castellanos (2007), we assume that advection with a given velocity is the predominant transport mechanism. If $v_{v/c}$ is the respective velocity of advection, the advective flux per unit width is

$$q_{v/c} = u_{v/c} v_{v/c}. \tag{3}$$

Note that the symbol q was used in Sect. 1 for the discharge of rivers. However, discharges will be expressed in terms of their catchment-size equivalent A_{eq} (Eq. 2) throughout this paper, so that it is not a problem to use q for the fluxes in the atmosphere in the following.

In a general formulation, $q_{v/c}$ and $v_{v/c}$ would be vectors in direction of advection. Let us, for simplicity, assume that the coordinate system is aligned in such a way that advection acts in x-direction. In addition, we assume dispersion in y-direction, i.e., in direction normal to the advection. Then the balance equation for each of the components reads

$$\frac{\partial u_{v/c}}{\partial t} = -\frac{\partial}{\partial x} q_{v/c} + \frac{\partial}{\partial y} \left(L_d v_{v/c} \frac{\partial u_{v/c}}{\partial y} \right) + s_{v/c}, \tag{4}$$

where $s_{v/c}$ is a source term describing the interaction between the components and the loss by precipitation. The dispersion length L_d is assumed to be the same for both components, although different values could also be used. Dispersion is the only process that links points with different y values. Without transversal dispersion, the precipitation pattern would fall into a set of individual lines parallel to the x axis. So transversal dispersion is an essential component of the approach in combination with two-dimensional landform evolution models. In turn, longitudinal dispersion could also be included, but we will see in Sect. 3 that it would make the numerical treatment more complicated and in Sect. 4.1 that it is not essential. Therefore, longitudinal dispersion is not taken into account.

Since the time scales of processes in the atmosphere are much shorter than the time scales involved in landform evolution, steady-state conditions can be assumed in Eq. (4). If we furthermore assume that the velocities are constant, Eq. (4) can be written conveniently in terms of the fluxes per unit width (Eq. 3):

$$-\frac{\partial q_{v/c}}{\partial x} + L_d \frac{\partial^2 q_{v/c}}{\partial y^2} + s_{v/c} = 0. \tag{5}$$

Following the concepts Smith and Barstad (2004), we assume that condensation (from u_v to u_c) and precipitation (from u_c) are linear processes with given time constants τ_c and τ_f, respectively. In contrast to this model and also to the model of Garcia-Castellanos (2007), we do not introduce an equilibrium water content explicitly. Instead, we start from a more fundamental level by considering condensation of vapor and re-evaporation of cloud water (e.g., Roe, 2005) as competing processes in the form

$$s_v = -\frac{u_v - \alpha u_c}{\tau_c}. \tag{6}$$

The nondimensional coefficient α defines the dynamic equilibrium between the two processes. An equilibrium between u_c and u_v is achieved if $\frac{u_v}{u_c} = \alpha$. Rewriting Eq. (6) in terms of fluxes per width yields

$$s_v = -\frac{q_v - \beta q_c}{L_c}, \tag{7}$$

with the length scale of condensation $L_c = v_v \tau_c$ and the modified coefficient $\beta = \frac{v_v}{v_c} \alpha$.

125   The rate of precipitation can also be expressed in terms of the flux per unit width according to

$$P = \frac{u_c}{\tau_f} = \frac{q_c}{L_f}, \tag{8}$$

with the length scale $L_f = v_c \tau_f$. Then the source term of u_c is

$$s_c = -s_v - P = \frac{q_v - \beta q_c}{L_c} - \frac{q_c}{L_f}. \tag{9}$$

and the full system of differential equations for the two fluxes reads

$$130 \quad -\frac{\partial q_v}{\partial x} + L_d \frac{\partial^2 q_v}{\partial y^2} - \frac{q_v - \beta q_c}{L_c} \qquad\qquad = 0 \tag{10}$$

$$-\frac{\partial q_c}{\partial x} + L_d \frac{\partial^2 q_c}{\partial y^2} + \frac{q_v - \beta q_c}{L_c} \quad -\frac{q_c}{L_f} = 0. \tag{11}$$

2.2 The effect of topography

Orographic precipitation is related to a dependence of the equilibrium on altitude (e.g., Roe, 2005). Since the re-evaporation of cloud water requires energy, altitude has an immediate effect here. The rate of re-evaporation should decrease with decreasing

135   temperature and thus with increasing altitude. As the simplest approach, we consider only this effect and assume that the length scales of condensation (L_c) and fallout (L_f) are constant. The Arrhenius relation

$$\beta \sim e^{-\frac{a}{T}} \tag{12}$$

with a constant a provides the simplest model for the dependence of β on the temperature T. Using a linear decrease of temperature with altitude H,

$$140 \quad T = T_0 - \Gamma H, \tag{13}$$

where T_0 is the temperature at sea level and Γ the lapse rate, Eq. (12) can be written in the form

$$\frac{\beta}{\beta_0} = e^{-\frac{a}{T_0 - \Gamma H} + \frac{a}{T_0}} \tag{14}$$

$$= e^{-\frac{a\Gamma H}{T_0(T_0 - \Gamma H)}} \tag{15}$$

$$\approx e^{-\frac{a\Gamma}{T_0^2} H}, \tag{16}$$

145   where β refers to the altitude H and β_0 to sea level. If we assume for simplicity that Eq. (16) also holds for the vertically integrated cloud water content with H as the surface height, we obtain the relation

$$\beta = \beta_0 e^{-\frac{H}{H_0}}, \tag{17}$$

where $H_0 = \frac{T_0^2}{a\Gamma}$ is a lumped parameter. It defines a vertical length scale and describes the height where β has decreased by a factor e compared to sea level. While the description of the height-dependence by a single, lumped parameter is convenient,

150   it is not an essential part of our model. Any other relation, e.g., the more elaborate version used by Garcia-Castellanos (2007) could be used as well.

2.3   Boundary conditions

Since the system of differential equations defined by Eqs. (10) and (11) is of first order in x and of second order in y, it is a parabolic system. Finding a unique solution in a rectangular domain ($0 \le x \le x_{\mathrm{max}}$, $0 \le y \le y_{\mathrm{max}}$) requires boundary

155   conditions at $x = 0$, $y = 0$, and $y = y_{\mathrm{max}}$ (but not at $x = x_{\mathrm{max}}$).

Since moisture is coming in at $x = 0$, it is straightforward to define q_{v} and q_{c} there. Then the integral of the total influx $q = q_{\mathrm{v}} + q_{\mathrm{c}}$ over this boundary defines the total amount of water available for precipitation in the domain. However, the question how to distribute a given total influx q to q_{v} and q_{c} is not trivial and requires more knowledge about the properties of the model. It will be addressed in Sect. 4.1.

160   All types of boundary conditions could be used at $y = 0$, and $y = y_{\mathrm{max}}$. Neumann boundary conditions or periodic boundary conditions are more useful than Dirichlet boundary conditions here since the q_{v} and q_{c} are fluxes along these boundaries, and it is not trivial to define reasonable prescribed values for q_{v} and q_{c}. Homogeneous Neumann boundary conditions define $\frac{\partial q_{\mathrm{v/c}}}{\partial y} = 0$, which means that there is no transversal dispersion across these boundaries. The implementation in the landform evolution OpenLEM presented in the following section uses periodic boundary conditions in y direction by default, which are

165   convenient in many applications.

3   Numerical implementation

Taking into account advection only along one for the coordinate axis and neglecting longitudinal dispersion considerably facilitates the numerical implementation of the model. Let us first rewrite Eqs. (10) and (11) in matrix form

$$-\frac{\partial \boldsymbol{q}}{\partial x} + L_{\mathrm{d}}\frac{\partial^2 \boldsymbol{q}}{\partial y^2} - \frac{1}{L_{\mathrm{c}}}\mathbf{A}\boldsymbol{q} = 0, \tag{18}$$

170   where

$$\boldsymbol{q} = \begin{pmatrix} q_{\mathrm{v}} \\ q_{\mathrm{c}} \end{pmatrix}, \quad \mathbf{A} = \begin{pmatrix} 1 & -\beta \\ -1 & \beta + \phi \end{pmatrix}, \quad \text{and} \quad \phi = \frac{L_{\mathrm{c}}}{L_{\mathrm{f}}}. \tag{19}$$

Let us further assume unit grid spacing in both directions, $\delta x = \delta y = 1$, for simplicity. This means that the length scales L_{d} and L_{c} must be measured in terms of the grid spacing in the following. If we use a left-hand (so upwind) difference quotient for the advection term, the discretized form of Eq. (18) can be written in the form

175   $$-\boldsymbol{q}_{x,y} + L_{\mathrm{d}}\left(\boldsymbol{q}_{x,y-1} - 2\boldsymbol{q}_{x,y} + \boldsymbol{q}_{x,y+1}\right) - \frac{1}{L_{\mathrm{c}}}\mathbf{A}\boldsymbol{q}_{x,y} = -\boldsymbol{q}_{x-1,y}, \tag{20}$$

where the indices x and y correspond to the positions. So the values $\boldsymbol{q}_{x,\cdot}$ can be computed from the values $\boldsymbol{q}_{x-1,\cdot}$ by solving a one-dimensional problem (in y direction). The respective linear equation has a tridiagonal structure of 2×2 blocks and can be written in the form

$$-L_\mathrm{d}\boldsymbol{q}_{x,y-1} + \mathbf{D}\boldsymbol{q}_{x,y} - L_\mathrm{d}\boldsymbol{q}_{x,y+1} = \boldsymbol{q}_{x-1,y} \tag{21}$$

180 with the 2×2-matrix

$$\mathbf{D} = (1 + 2L_\mathrm{d})\,\mathbf{1} + \frac{1}{L_\mathrm{c}}\mathbf{A} \tag{22}$$

and the 2×2 identity matrix $\mathbf{1}$. This equation system can be solved, e.g., by the direct Gaussian scheme based on 2×2 blocks.

The examples shown in the following section are computed using the open-source landform evolution model OpenLEM. This model already contains up-to-date implementations of fluvial erosion such as the shared stream-power model (Hergarten, 185 2020), which will be used in Sect. 7. All components of OpenLEM are of linear time complexity at arbitrary time step lengths, which means that the numerical effort increases only linearly with the size of the lattice. The computation of the precipitation proposed here preserves this property. Independently of the size of the lattice, we found an increase in computing time by a factor of about 2.4 compared to the simplest form of the SPIM and a factor of about 2.2 compared to the shared stream-power model, which includes sediment transport. This increase is owing to taking into account transversal dispersion, where Neumann 190 boundary conditions would be cheaper than the periodic boundary conditions used in OpenLEM.

4   Fundamental properties of the model

4.1   Characteristic length scales

Let us for the moment consider the model only in longitudinal direction, i.e., without the dispersion term, and let us assume a constant height for the moment. Then the set of parameters consists of two horizontal length scales L_c and L_f and a nondi-195 mensional parameter β. In this section, it is shown that the relevant length scales that characterize the properties of the model differ from L_c and L_f.

In this situation, Eq. (18) reduces to a linear system of two ordinary differential equations,

$$\frac{\partial \boldsymbol{q}}{\partial x} = -\frac{1}{L_\mathrm{c}}\mathbf{A}\boldsymbol{q}. \tag{23}$$

The behavior of the solutions are determined by the eigenvalues of the matrix $\mathbf{A}$ defined in Eq. (19). These are found by solving 200 the characteristic equation of $\mathbf{A}$,

$$\lambda^2 - (1 + \beta + \phi)\,\lambda + \phi = 0, \tag{24}$$

which yields

$$\lambda_\pm = \frac{1 + \beta + \phi}{2} \pm \sqrt{\left(\frac{1 + \beta + \phi}{2}\right)^2 - \phi}. \tag{25}$$

The eigenvalues describe exponentially decaying solutions of the form $e^{-\frac{\lambda_\pm}{L_c}x}$. These solutions can also be written in the form

205 $e^{-\frac{x}{L_1}}$ and $e^{-\frac{x}{L_s}}$, respectively, where

$$L_1 = \frac{L_c}{\lambda_-} \quad \text{and} \quad L_s = \frac{L_c}{\lambda_+}. \qquad (26)$$

Since $\lambda_- \leq 1$ and $\lambda_- \leq \phi$ for all values of β and ϕ,

$$L_1 > \max\{L_c, L_f\} \qquad (27)$$

for $\beta > 0$. In turn, $\lambda_- \lambda_+ = \phi$, and thus

210 $$L_1 L_s = L_c L_f. \qquad (28)$$

As a consequence,

$$L_s < \min\{L_c, L_f\} \qquad (29)$$

for $\beta > 0$. So the approach based on the dynamic equilibrium creates two characteristic length scales outside the range between L_c and L_f. These scales differ even if we assume $L_c = L_f$ as suggested by Smith and Barstad (2004).

215 The longer length scale L_1 describes the ability to transport moisture over large distances. Smith and Barstad (2004) suggested time scales of 200 s to 2000 s for the conversion of cloud water and for fallout, corresponding to length scales L_c and L_f of 10 km to 100 km at wind speeds of 50 ms^{-1}. If we, e.g., assume $\beta = 10$, L_1 is in the range between 119 km and 1191 km. So the transport range may be considerably larger than the length scales L_c and L_f of the involved processes. This property is essential for simulating long-range transport over large continental areas with a closed water balance.

220 The mode of long-range transport is obtained by inserting λ_- into the first row of the eigenvalue equation $\mathbf{A}\boldsymbol{q} = \lambda \boldsymbol{q}$,

$$q_v - \beta q_c = \lambda_- q_v, \qquad (30)$$

and thus

$$\frac{q_c}{q_v} = \frac{1 - \lambda_-}{\beta} = \frac{1 - \frac{L_c}{L_1}}{\beta} = \frac{1}{\frac{L_1}{L_f} - 1}. \qquad (31)$$

According to Eq. (7), this ratio is $\frac{q_c}{q_v} = \frac{1}{\beta}$ in equilibrium. So the vapor content is slightly above its equilibrium value in the

225 long-range transport mode, which results in a low net rate of condensation.

Figure 1 illustrates the long-range transport for a boxcar-shaped topography with a height $H = H_0$. All properties are considered as nondimensional values. The parameter values are $L_c = L_f = 1$, and $\beta_0 = 10$. The incoming fluxes are $q_v = 10$ and $q_c = 0$ at $x = 0$. According to Eqs. (25) and (27), the length scale of long-range transport is $L_1 \approx 11.9$ at sea level ($H = 0$). Both fluxes and the rate of precipitation decrease exponentially with this length scale for $x < 5$ and $x > 10$, except for the

230 beginning of the ranges.
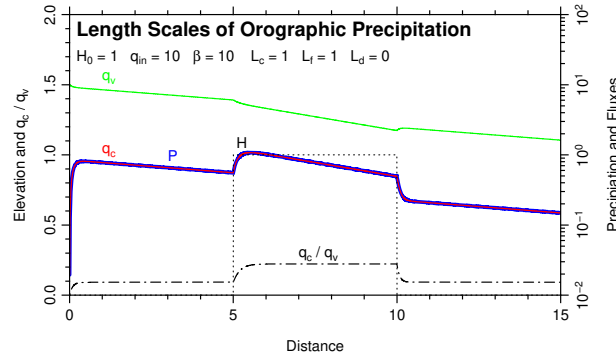
Figure 1. Principal properties of the model in 1D for a boxcar-shaped topography. Fluxes and precipitation rates are shown on logarithmic axes in order to emphasize the exponential decrease.

The plateau ($H = H_0$) is characterized by a lower value of $\beta = e^{-1} \approx 0.37$ according to Eq. (7), resulting in a lower length scale $L_l \approx 5.5$. So the precipitation is higher at the plateau, but in turn decreases more rapidly with x. This difference is reflected in a lower ratio $\frac{q_c}{q_v}$, so in a lower ability to keep moisture in form of vapor.

In turn, the short length scale L_s describes the adjustment if the ratio of q_c and q_v deviates from Eq. (31). Since these
235 deviations predominantly arise from changes in topography (via the height-dependence of β), the length scale L_s can be considered as the length scale of orographic precipitation.

Three transitions zones characterized by L_s occur in Fig. 1, starting at $x = 0$, $x = 5$, and $x = 10$, respectively. The length scale of the first and the third transition ($H = 0$) is $L_s \approx 0.08$, while it is $L_s \approx 0.18$ for the second transition ($H = H_0$). In general, L_s increases with elevation, while the length scale of long-range transport L_l decreases with elevation. Their product
240 is constant according to Eq. (28).

While the second and the third transition arise from changes in topography, the first transition occurs because it is assumed that the influx only contains vapor ($q_v = 10$), but no cloud water ($q_c = 0$), which is far off from equilibrium and from the long-range transport mode. It is therefore useful to adjust the boundary condition in such a way that the incoming fluxes are in the long-range transport mode described by Eq. (31). Then the incoming flux of cloud water must be

$$245 \quad q_c = q \frac{L_f}{L_l}, \tag{32}$$

where q is the total incoming flux, and $q_v = q - q_c$. This modified boundary condition is used in all subsequent examples throughout this study.

The non-instantaneous reaction to abrupt changes in topography is a central property of the model. Without this, the small-scale roughness of topography would directly affect the precipitation pattern, so that an additional smoothing procedure would
250 be required. Longitudinal dispersion could also used for smoothing, but as our model generates a scale of smoothing on its own, taking into account longitudinal dispersion is not urgently required. Taking this result into account, our approach based
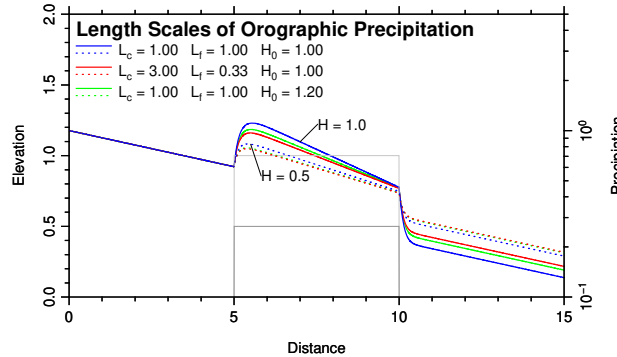
Figure 2. Effect of L_c and L_f, where L_l (at sea level) and the product $L_c L_f$ were kept constant. The solid lines refer to the original scenario ($H = 1$) and the dashed lines to a reduced topography ($H = 0.5$). The results for $L_c = \frac{1}{3}$ and $L_f = 3$ are practically the same as for $L_c = 3$ and $L_f = \frac{1}{3}$.

on two components of water content with a two-way conversion is some kind of minimum model that is able to capture both continentality (a slow decrease in precipitation at large scales) and a delayed reaction to small-scale changes in topography.

255 While the model in its original form involves two longitudinal length scales L_c and L_f, a transversal length scale L_d, a vertical length scale H_0, and a nondimensional parameter β_0 (referring to sea level), it is also possible to replace β_0 by the length scale of long-range transport L_l (alternatively also by L_s, but that would be less useful). The value of β can be computed conveniently from Eq. (24):

$$\beta = \frac{\lambda^2 + \phi}{\lambda} - \phi - 1 \tag{33}$$

$$= \left(1 - \frac{L_c}{L_l}\right)\left(\frac{L_l}{L_f} - 1\right). \tag{34}$$

260 While this relation is valid for the respective values of L_l and β at any height, it is particularly useful for computing β_0 from L_c, L_f, and L_l at sea level.

If we use L_l instead of β_0, Eq. (28) reveals that the short length scale L_s only depends on L_l and on the product $L_c L_f$, while the individual values of L_c and L_f are not relevant for L_s at sea level. This is, however, not the case for the height-dependence. Figure 2 illustrates the relevance of the individual values of L_c and L_f in combination with topography. The default scenario

265 (solid blue line) is the same as in Fig. 1, except that the fluxes at the boundary were adjusted according to Eq. (32). In all scenarios, L_l (at sea level) was kept constant (so not β_0). As expected, the behavior at sea level remains the same for $L_c \neq L_f$ (red lines) as long as the product $L_c L_f$ is constant. This is, however, not true at $H > 0$, where the increase in precipitation with height becomes distinctly weaker for $L_c \neq L_f$ (red vs. blue lines), regardless which of the values is greater.

The decrease in L_l with height and thus the respective increase in precipitation can be computed from Eq. (17) according to

270
$$\frac{dL_l}{dH} = \frac{d\beta}{dH}\frac{dL_l}{d\beta} = \frac{\beta}{H_0}\frac{L_c}{\lambda_-^2}\frac{d\lambda_-}{d\beta}. \tag{35}$$

The remaining derivative can be computed from Eq. (24),

$$\frac{d\lambda_-}{d\beta} = \frac{\lambda_-}{2\lambda_- - (1 + \beta + \phi)} = -\frac{\lambda_-}{\lambda_+ - \lambda_-}. \tag{36}$$

Inserting this result into Eq. (35) yields

$$\frac{dL_l}{dH} = -\frac{\beta}{H_0} \frac{L_f L_l}{L_l - L_s} \tag{37}$$

after some basic transformations, and finally after inserting Eq. (34)

$$\frac{dL_l}{dH} = -\frac{1}{H_0} \frac{(L_l - L_c)(L_l - L_f)}{L_l - L_s}. \tag{38}$$

It is easily recognized that the second factor is always lower than L_l. So the decrease in L_l and thus the increase in precipitation with height is always smaller than the decrease in β, which is characterized by the vertical scale H_0. The relation is symmetric concerning L_c and L_f, and the height-dependence is strongest for $L_c = L_f = \sqrt{L_l L_s}$.

At least for topographies with moderate relief (in relation to H_0), a difference between L_c and L_f can be replaced by an increased value of H_0. If we define

$$\tilde{L}_c = \tilde{L}_f = \sqrt{L_c L_f} \quad \text{and} \quad \tilde{H}_0 = \frac{(L_l - \tilde{L}_c)^2}{(L_l - L_c)(L_l - L_f)} H_0, \tag{39}$$

the behavior of the model essentially remains the same for moderate heights. This result is illustrated by the green lines in Fig. 2. The precipitation obtained for $L_c = L_f = 1$ with and increased reference height $H_0 = 1.2$ (Eq. 39) are close to those for $L_c = 3$ and $L_f = \frac{1}{3}$ with $H_0 = 1$ for the topography with $H = \frac{1}{2}$. For the higher topography with $H = 1$, however, the remaining deviation is larger.

Keeping in mind that the definition of H_0 in Sect. 2.2 already required some approximations, it is not a problem that H_0 has to be increased artificially if we replace different values of L_c and L_f by the same value $\sqrt{L_c L_f}$. If we accept that there is a residual overestimation of the effect of topography that increases with surface height, we can assume $L_c = L_f$ without losing much of the model's fundamental capabilities.

4.2 The influence of transversal dispersion

As mentioned above, transversal dispersion is the only component that prevents the model from falling into a set of independent one-dimensional models. In contrast to the other length scales of the model, however, the dispersion length cannot be interpreted directly as a spatial scale. It rather links longitudinal and transversal length scales of the moisture pattern.

Let us for the moment assume that condensation and fallout are switched off ($L_c = L_f \to \infty$) and that the topography is flat ($H = 0$). Let us further assume that the incoming flux (at $x = 0$) has some transversal variation in water content (either in q_v or q_c or in both) according to

$$\delta q(0, y) = \sin\left(\frac{\pi y}{L_y}\right), \tag{40}$$

Orographic Precipitation Considering Transversal Dispersion

(a) Dispersion Length (L_d) = 0   (b) Dispersion Length (L_d) = 0.01   (c) Dispersion Length (L_d) = 0.1
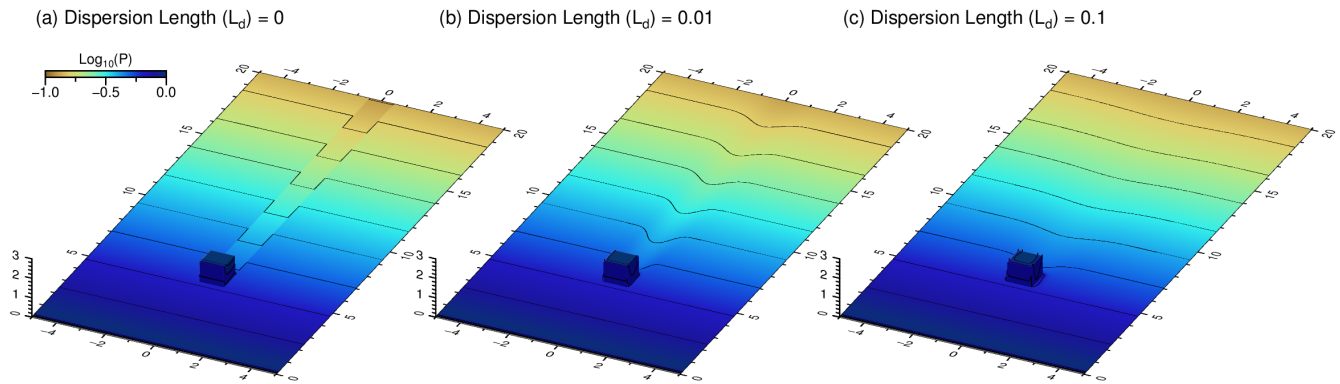
Figure 3. Effect of transversal dispersion on the precipiation behind an obstacle.

where L_y defines the length scale of this variation (half of the wavelength). Then Eq. (10) (or alternatively Eq. 11) yields

$$\delta q(x,y) = \delta q(0,y) e^{-\frac{x}{L_x}}, \tag{41}$$

with

$$L_x = \frac{L_y^2}{\pi^2 L_d}. \tag{42}$$

So small-scale transversal patterns decay much faster in direction of advection than large-scale patterns. The length scale of the decay, L_x, decreases quadratically with the scale L_y of the transversal pattern. The length scale of dispersion, L_d, describes the strength of dispersion, so that an increase in L_d reduces L_x.

Figure 3 illustrates the effect of dispersion for an obstacle of a width $L_y = 1$ and a height $H = 1$, where the parameter values are the same as in the previous examples. Without transversal dispersion ($L_d = 0$), the higher precipitation falling on the obstacle causes an infinite precipitation shadow. For $L_d = 0.01$, the longitudinal scale of decay is $L_x \approx 10$ (Eq. 42). The precipitation shadow has become considerable weaker at this distance behind the obstacle, but is still visible. Finally, the scale of decay decreases to $L_x \approx 1$ for $L_d = 0.1$, so that the shadow vanishes rapidly behind the obstacle.

5 Extension by evapotranspiration

Evaporation including the transpiration by plants, called evapotranspiration, plays a major part in the water balance. While the potential rate of evapotranspiration mainly depends on the climatic conditions and on vegetation, the actual rate is often much lower due to limited availability of water at the surface and in the shallow subsurface.

However, the concept for including variations in precipitation in large-scale landform evolution models is not able to predict the availability of water. The water balance is stated in terms of fluxes, which are not directly related to amounts of stored water. Estimating the amount of stored water would require a model for the flow velocity and would introduce additional

complexity. Garcia-Castellanos (2007) presented a first step in this direction by distinguishing lake areas and assigning a rate of precipitation to these areas.

320 Here we propose a simpler idea by assuming that the rate of evapotranspiration is proportional to the rate of precipitation instead of the amount of stored water. This means that a given fraction ϵ of the precipitation evaporates immediately. This leads to one additional term in Eq. (10), so that the system of differential equations turns into

$$-\frac{\partial q_\text{v}}{\partial x} + L_\text{d}\frac{\partial^2 q_\text{v}}{\partial y^2} - \frac{q_\text{v} - \beta q_\text{c}}{L_\text{c}} + \quad \epsilon \quad \frac{q_\text{c}}{L_\text{f}} = 0 \tag{43}$$

$$-\frac{\partial q_\text{c}}{\partial x} + L_\text{d}\frac{\partial^2 q_\text{c}}{\partial y^2} + \frac{q_\text{v} - \beta q_\text{c}}{L_\text{c}} - \quad \frac{q_\text{c}}{L_\text{f}} = 0 \tag{44}$$

325 While the total precipitation is still $P = \frac{q_\text{c}}{L_\text{f}}$, the effective precipitation that contributes to runoff is

$$P_\text{eff} = (1-\epsilon)P = (1-\epsilon)\frac{q_\text{c}}{L_\text{f}} \tag{45}$$

then.

In order to understand the effect of evapotranspiration, Eqs. (43) and (44) can be brought to the same form as Eqs. (10) and (11) by introducing an increased coefficient for re-evaporation in the atmosphere

330 $$\tilde{\beta} = \beta + \epsilon\frac{L_\text{c}}{L_\text{f}} \tag{46}$$

and an increased fallout length

$$\tilde{L}_\text{f} = \frac{L_\text{f}}{1-\epsilon}. \tag{47}$$

Then ϕ (Eq. 19) changes to

$$\tilde{\phi} = (1-\epsilon)\phi. \tag{48}$$

335 It is easily recognized that $\tilde{\beta} + \tilde{\phi} = \beta + \phi$. So only the last term ϕ in Eq. (25) is affected by evapotranspiration. The smaller eigenvalue λ_- comes closer to zero then, while the greater eigenvalue λ_+ does not change much. So L_l increases considerably, while L_s remains almost constant, and thus

$$\tilde{L}_\text{l} \approx \frac{L_\text{l}}{1-\epsilon} \tag{49}$$

according to Eq. (28).

340 While these results suggest that the effect of evapotranspiration could be mimicked by modifying the parameters β and L_f (Eqs. 46 and 47), it must be kept in mind that this only holds at constant elevation. Otherwise, β depends on H, and thus also the effect of ϵ on L_l. Since β describes the re-evaporation of water in the atmosphere, it makes sense to assume that the rate of evapotranspiration has the same dependence on H as β,

$$\epsilon = \epsilon_0 e^{-\frac{H}{H_0}}, \tag{50}$$
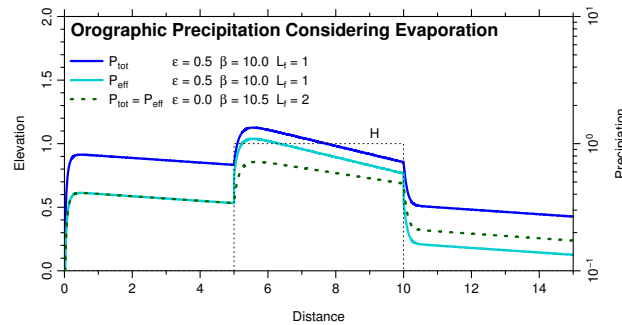
Figure 4. Effect of elevation-dependent evaporation on precipitation.

although ϵ refers to the surface and β to height-integrated properties.

Then the dependence of Eq. (46) remains valid for all heights. However, as ϵ decreases with height, the increase in the effective L_f (Eq. 47) and thus also in the effective L_l becomes weaker at large elevations. So mimicking evapotranspiration by adjusting β and L_f (Eqs. 46 and 47) would overestimate the effect of evaporation at large elevations or, in turn, underestimate the effect of elevation. Figure 4 illustrates this result for the example from Fig. 1, where an evaporation ratio $\epsilon_0 = 0.5$ is assumed at sea level. The results are compared to the model without evaporation, but with modified parameter values $\tilde{\beta} = 10.5$ (Eq. 46) and $\tilde{L}_f = 2$ (Eq. 47). The effective precipitation in the mountain region and the effective length scale of transport differ by almost a factor of two for $H = H_0$. So mimicking evapotranspiration by adjusted parameters is only useful for small topography.

6 Comparison to existing models

As discussed in Sect. 1, the models of Smith and Barstad (2004) and Garcia-Castellanos (2007) also use vertically integrated water contents and advective transport at a given wind velocity. In its spirit, our approach is somewhat similar to these models.

It may seem first that taking into account transversal dispersion was the major progress of our approach. However, the numerical scheme proposed in Sect. 3 could in principle also be used for including transversal dispersion in the two other models. The fundamental differences are hidden in details of the model structure that have a bigger effect than it seems first.

The model of Smith and Barstad (2004) assumes only a one-way coupling between the two moisture components. In the terminology of our model, this would be $\beta = 0$ in Eqs. (10) and (11). Following the considerations of Sect. 4.1, the length scale of long-range transport of moisture is $L_l = \max\{L_c, L_f\}$ then, which is between about 10 km and 100 km at rather high wind speeds of 50 ms^{-1}. So assuming a one-way conversion practically removes the ability to transport moisture over large distances of several hundred km. Smith and Barstad (2004) fixed this problem by assuming a permanent refilling of the water storages at some given background rate. So this model focuses on the behavior at intermediate scales, but cannot capture large-scale precipitation patterns. This is presumably the reason why the two moisture components are interpreted as cloud water and hydrometeors by Smith and Barstad (2004) instead of vapor and cloud water in our model.

Beyond this, it must also be noted that the feedback parameter β carries the information about the height-dependence in our model. So the effect of topography must be included in another way if this feedback is not taken into account. Smith and

370 Barstad (2004) assumed that the rate of conversion is not proportional to the absolute value of the cloud water content (q_v in our model), but to the difference of this content towards a height-dependent equilibrium content. This results in an additional source or sink term in the equations, which may even cause negative precipitation rates at the leeward side of a mountain. In order to overcome this problem, Smith and Barstad (2004) suggested to truncate the precipitation term explicitly at negative values. Without this truncation, this model would even be linear not only concerning the water contents (like our model), but also

375 concerning the surface height H. The truncation, however, even destroys the linearity with regard to the water contents, which costs much of the model's simplicity, in particular if an extension by transversal dispersion is desired. In contrast, Eqs. (10) and (11) of our model are homogeneous, i.e., contain no external source or sink terms. As long as $\beta \geq 0$, it is guaranteed that neither q_v nor q_c can become negative. So our model requires no artificial truncation in order to avoid negative precipitation rates.

380 In this sense, including the feedback by re-evaporation in our approach may look more complicated first, but it is the key to capturing large-scale precipitation patterns and avoids the need for taking additional measures against negative precipitation rates.

The model of Garcia-Castellanos (2007) uses a single moisture component and thus seems to be simpler than our approach. The fundamental structure of this model can be explained by considering the limit $L_c \to 0$. This means that the contents of

385 vapor and cloud water immediately achieve an equilibrium $\frac{q_v}{q_c} = \beta$, defined by the height-dependent value β. Adding Eqs. (10) and (11) then yields

$$-\frac{\partial q}{\partial x} + L_d \frac{\partial^2 q}{\partial y^2} - \frac{q}{(1+\beta)L_f} = 0, \tag{51}$$

where $q = q_v + q_c$ is the total flux per unit width. This is the fundamental structure of the model of Garcia-Castellanos (2007) except for the dispersion term. The precipitation rate is the ratio of q and a height-dependent value $(1+\beta)L_f$. The length scale

390 of transport is $L_l = (1+\beta)L_f$ then, which is much larger than L_f if β is sufficiently large. So replacing the coupling between the two flux components by an equilibrium preserves the ability to capture large-scale precipitation dynamics.

However, the short length scale L_s is lost if we assume instantaneous equilibrium. Precipitation reacts immediately to changes in topography then, so that the precipitation pattern becomes sensitive to the small-scale roughness. In order to overcome this problem, Garcia-Castellanos (2007) introduced an additional smoothing by applying a convolution with half of a

395 Gaussian curve in upwind direction. As illustrated in Fig. 5, the behavior of the one-component version with additional smoothing is indeed similar to our two-component approach in 1D. Here, a smoothing length $\Delta x = 2L_s$ appears to be a reasonable choice at $H = 0$. However, it should be emphasized that the concept of smoothing including the choice of a smoothing length is an ad-hoc assumption, while smoothing automatically emerges in our two-component model. Beyond this, applying the convolution with half of a Gaussian function is numerically more expensive than the treatment of two moisture components.

400 In this sense, considering two moisture components is indeed the simplest choice if we want to combine long-range transport and a smooth response to sharp topographic gradients in a linear model. This result is directly related to the occurrence of two
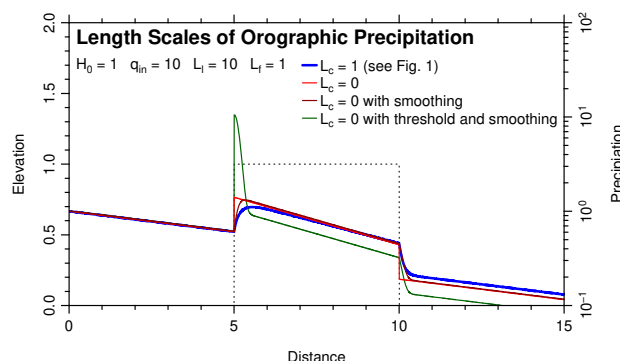
Figure 5. Comparison of our approach to the one-component model of Garcia-Castellanos (2007). The parameter values are the same as in Fig. 1.

eigenvalues, i.e., horizontal length scales discussed in Sect. 4.1. A single-component model seems to be simpler at first sight, but we have to pay for this simplicity later as soon as we need the second length scale.

Moreover, the model of Garcia-Castellanos (2007) contains a nonlinear component, which is not included in our approach. While the precipitation term $\frac{q}{(1+\beta)L_{\mathrm{f}}}$ in Eq. (51) was obtained by simplifying out two-component model, Garcia-Castellanos (2007) introduced an expression with this structure directly in the form

$$P = P_0 \frac{u}{u_{\max}(H)}, \tag{52}$$

where P_0 is some reference precipitation, $u_{\max}(H)$ is a height-dependent maximum water content. While this expression is still equivalent to the precipitation term in Eq. (51), it was extended in such a way that Eq. (52) is only applied for $u < u_{\max}(H)$. Otherwise, it was assumed that the excess water content $u - u_{\max}(H)$ is immediately converted into precipitation. Transferred to the formalism of Eq. (51), this occurs if the ratio $\frac{q}{1+\beta}$ exceeds a given threshold.

The green curve in Fig. 5 illustrates this effect, where it was assumed that the air at the left-hand boundary is just at the limit $u = u_{\max}(0)$. While $u < u_{\max}(0)$ in the foreland, $u_{\max}(H)$ (via $1+\beta$ in our formalism) decreases suddenly at $x = 5$ due to the sudden increase in H, so that $u > u_{\max}(H)$. This would even result in a sharp peak in the precipitation curve without smoothing. Smoothing in upstream direction reduces the height of the peak and widens it into the plateau.

As a main effect of this extension, the model becomes able to predict some kind of overshooting in precipitation at the windward side of mountains. For a high-altitude plateau, the original version predicts a gentle increase of precipitation to the level at the plateau. A decrease in precipitation only occurs due to the decrease in water content or, if we consider a mountain range, due to decreasing height at the leeward side.

Such an effect might be useful, although the physical basis is not trivial since a dynamic equilibrium between vapor and cloud water is already included in the linear model. Our linear two-component model could be extended by nonlinearity in several ways. The precipitation process may be a candidate here since coagulation plays a part in the growth of hydrometeors,

and the rate of coagulation increases rather quadratically than linearly with concentration. However, following the concept of parsimony, we do not follow ideas of nonlinearity further in this study.

7 Examples

Similarly to the approaches of Roe et al. (2003), Smith and Barstad (2004), and Garcia-Castellanos (2007), the scope of the model developed in this study is not a precise prediction of precipitation rates, but its combination with long-term landform evolution. This section provides some examples exploring the effect of orographic precipitation and continentality on fluvial landform evolution and the feedback of the resulting topography on the precipitation pattern.

As described in Sect. 1, the SPIM and its derivates can easily be extended by a variable effective precipitation and thus be coupled with our model. In the following, we use a model that is not restricted to pure bedrock incision, but also takes into account sediment transport. While the idea behind this model dates back to Davy and Lague (2009) or partly even to older studies (Howard, 1994; Kooi and Beaumont, 1994), it is used here in the most recent formulation, the so-called shared stream-power model (Hergarten, 2020). The constitutive equation of the shared stream-power model reads

$$\frac{E}{K_\mathrm{d}} + \frac{Q}{K_\mathrm{t}A} = A^m S^n, \tag{53}$$

where Q is the sediment flux (volume per time). This model contains two erodibilities, where K_d describes the erodibility in absence of transported sediment, while K_t characterizes the ability to transport sediment at zero erosion. For spatially uniform erosion, the sediment flux is $Q = EA$, and Eq. (53) turns into the SPIM (Eq. 1) with an effective erodibility K according to

$$\frac{1}{K} = \frac{1}{K_\mathrm{d}} + \frac{1}{K_\mathrm{t}}. \tag{54}$$

Following Robl et al. (2017), we use $n = 1$ (i.e., the linear version of the model), $m = 0.5$, and $K = 2.5\ \mathrm{Myr}^{-1}$. Studies of natural and experimental river profiles at the transition to a foreland by Guerit et al. (2019) suggest a ratio $\frac{K_\mathrm{d}}{K_\mathrm{t}} \approx 1.6$ (G in their notation) for $n = 1$, which leads to $K_\mathrm{d} \approx 6.5\ \mathrm{Myr}^{-1}$ and $K_\mathrm{t} \approx 4.1\ \mathrm{Myr}^{-1}$.

The concept of expressing discharges as their catchment-size equivalent (referring to a hypothetic uniform reference precipitation rate) is particularly useful in the context of the shared stream-power model. If both occurrences of A in Eq. (53) are interpreted as catchment-size equivalents of the actual discharge, Eq. (53) remains formally the same, including the values and the units of K_d and K_t.

We use a regular mesh of 2000×2000 nodes for a domain of 500 km linear size, corresponding to a spatial resolution of 250 m. Although rather coarse, hillslope processes are still relevant at this scale. Using a purely fluvial model would lead to artificially steep slopes and thus increased heights at the drainage divides, which may affect the precipitation pattern despite the robustness of the model against the small-scale roughness of the topography. In order to avoid this, we use an approach that was brought into play in the context of debris flows in steep valleys by Stock and Dietrich (2003) and developed further by Hergarten et al. (2016). This approach replaces the term A^θ in Eq. (1) (or here in Eq. 53) where $\theta = \frac{m}{n}$ by $A^\theta + A_\mathrm{c}^\theta$, where A_c is a given constant. This modification acts like an increased catchment size or like an increased discharge and thus avoids the

occurrence of extremely steep slopes at small catchment sizes. We use $A_\mathrm{c} = 1$ pixel ≈ 0.06 km^2 here, which roughly consistent

455 with the estimate $A_\mathrm{c} = 0.05$ km^2 obtained by Hergarten et al. (2016) for the topography of Taiwan.

In the following section, we show how the decrease in precipitation rate with distance to the source of moisture (i.e., continentality) controls the shape and the height of large mountain ranges. Then we illustrate topographic patterns resulting from feedbacks between rock uplift, orographic precipitation, and fluvial erosion.

7.1 Impact of continentality on landform evolution

460 The large-scale precipitation pattern over continental areas is controlled by the length scale of long-range moisture transport L_l. If the extension of a mountain belt in wind direction reaches the order of magnitude of L_l, the precipitation pattern may have a strong influence on its height and shape even without any immediate effect of elevation on precipitation. In terms of the model parameters, this situation is described by a reference height H_0 much larger than the surface height. Then the precipitation pattern reflects increasing continentality with an exponential drop in precipitation rate from the moisture source towards the

465 continental inland. The precipitation rate is solely controlled by the influx q_in and the length scale L_l, which is further stretched by considering evaporation.

Figure 6 shows the effect of continentality on mountain topography. The considered mountain range is 300 km wide and uplifted at a rate of 0.25 km Myr^{-1} in all three examples. The two 100 km wide foreland regions are tectonically inactive. Moisture enters the model domain at the southern boundary and is advected towards north. While the geometry, the length

470 scales $L_\mathrm{c} = L_\mathrm{f} = 25$ km, the height-independent evaporation ratio $\epsilon = 0.5$, and the amount of moisture entering the southern boundary are the same in all three scenarios, the length scale L_l of the long-range transport varies from 50 km to 600 km. Only steady-state topographies are considered, where the term steady state is used in a sloppy way here since the drainage pattern in an inactive foreland permanently reorganizes (Yuan et al., 2019). Since this reorganization has a minor effect on the mountain topography, the mountain range comes close to a steady state with some fluctuations.

475 Two effects of continentality must be distinguished. First, L_l has an influence on the amount of precipitation that the mountain range receives in total. This amount should affect the total height of the steady-state mountain range. It is small if L_l is small since most of the moisture is already lost in the foreland, but also small if L_l is large since most of the moisture passes the domain without much precipitation then. So there must be a length L_l where the amount of precipitation on the mountain range becomes maximal.

480 For $L_\mathrm{l} = 600$ km (Fig. 6a,b), evaporation with $\epsilon = 0.5$ effectively stretches L_l to about 1200 km following the considerations of Sect. 5. Since this is four times the width of the mountain range, the precipitation rate varies by a factor of $e^{\frac{1}{4}} \approx 1.28$ over the mountain range. Differences in discharge are, however, smaller. If the drainage divide is in the middle, the difference in total precipitation differs only by a factor of $e^{\frac{1}{8}} \approx 1.13$ between the windward and the leeward half of the mountain range. So the discharges of the big rivers only differ by this factor at the edges of the mountain range.

485 This difference is visible in the swath profile (Fig. 6b). The distribution of maximum heights across the mountain ranges is already quite asymmetric since small catchment sizes at ridge lines and hillslopes cause erosion rate to be directly related to local precipitation rate. Hence, highest domains of the mountain range become increasingly steeper towards the leeward side.
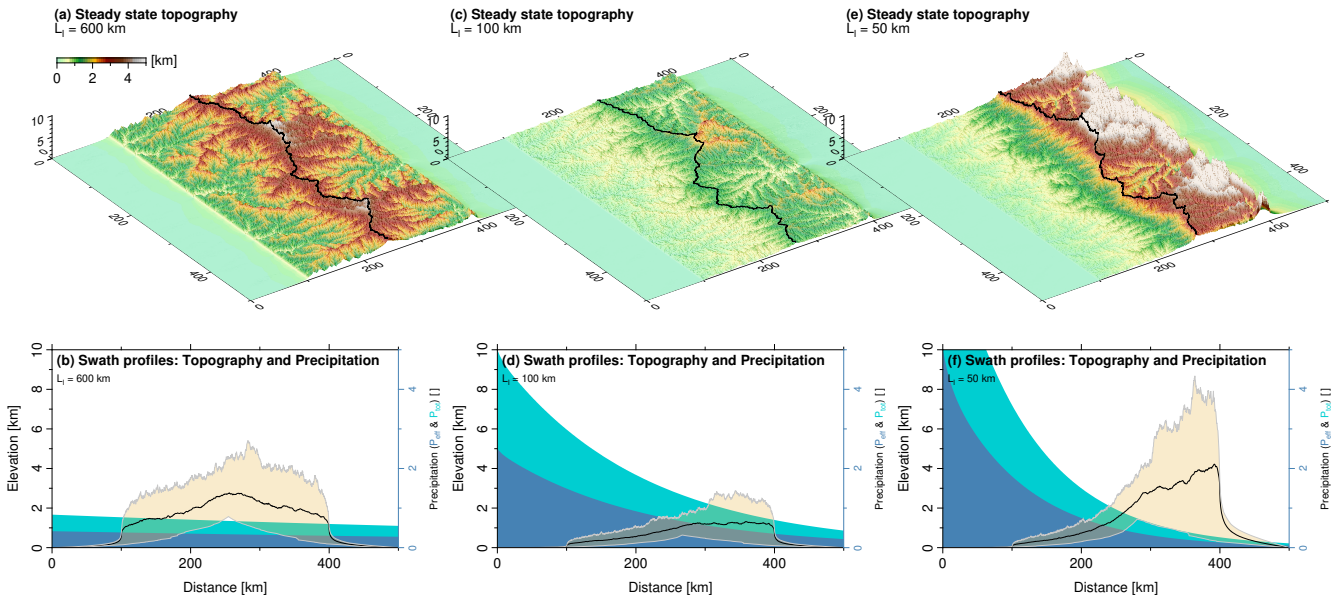
Figure 6. Continentality and steady-state mountain range geometry. Uplift rate ($U = 0.25$ km Myr^{-1}), erodibility ($K = 2.5$ Myr^{-1}) and factor of evaporation ($\epsilon = 0.5$) are the same in all three experiments. (a, c, e) show perspective views of steady state mountain topography for $L_l = 50$ km, 100 km and 600 km, respectively. The black solid line indicates the main drainage divide separating the windward from the leeward side of the mountain range. (b, d, f) are south-north trending swath profiles representing total precipitation (turquoise area) and effective precipitation (blue area) and topography (brown) with average (thick solid line) and extreme values (thin solid lines) taken over the full west-east extent of the model domain.

In contrast, the minimum height of the swath profiles describes the large rivers, which differ not so much in their discharge. So the profile of the minimum height is still quite symmetric here. This also implies that the relative incision of the rivers in
490   relation to the hillslopes is deeper at the leeward side than at the windward side.

According to the findings of Sect. 5, the length scale $L_l = 100$ km considered in Fig. 6(c,d) is stretched by evaporation to 206 km. This value is close to the length scale where the mountain range receives the maximum amount of precipitation in total, $\frac{300\text{km}}{\ln 4} = 216$ km. Consequently, the overall height of the mountain range is quite low here. Since precipitation varies by a factor of $e^{\frac{300}{206}} \approx 4.3$ here, the topography becomes strongly asymmetric. Again, this asymmetry mainly concerns the maximum
495   height in the swath profile (Fig. 6d), while the asymmetry of the minimum height referring to the largest rivers is smaller. Nevertheless, the asymmetry in the minimum height is clearly visible here, and it goes along with a shift of the principal drainage divide towards the leeward side. While the total area drained by the leeward part of the mountain range was 48 % of the total area of the mountain range for $L_l = 600$ km, this fraction has decreased to 42 % now. Despite this moderate shift, the highest peaks are already separated from the main drainage divide.

500   For $L_l = 50$ km (Fig. 6e,f, effectively 114 km with evaporation), the total amount of precipitation on the orogen decreases. This result in an increasing overall surface height. More importantly, the topography becomes extremely asymmetric since the

precipitation rate varies by a factor of $e^{\frac{300}{114}} \approx 14$ over the mountain range. This variation is strong enough to make the river profiles (minimum height in Fig. 6f) strongly asymmetric. The overall asymmetry is so strong that is also dominates the mean elevation. Apart from very high peaks close to the leeward border of the mountain range, the maximum mean elevation is also achieved there, while the version with $L_l = 100$ km featured an almost constant mean height over the leeward part of the mountain range. In turn, the shift of the main drainage divide is only moderate compared to the previous scenario. The leeward fraction of the total drained area has decreased from 42 % to 39 %. As a consequence, the large massifs that have formed in the northern part drain almost entirely towards the leeward side. So rivers starting from high regions partly drain towards south first, but then change their flow direction towards the large north-trending valleys.

7.2 Orographic precipitation controlling mountain range geometry

We finally consider the effect of topography on the precipitation pattern and the resulting feedback on landform evolution. The overall geometry and the parameter values are the same as before, except for a fixed length scale $L_l = 500$ km, which was chosen in such a way that the effect of continentality over the mountain range is rather weak. In contrast to the previous examples, transversal dispersion is relevant here, where $L_d = 5$ km was chosen.

While the vertical length scale could be defined arbitrarily based on the erodibility and the uplift rate in the previous examples, it is defined here by the reference height H_0 that describes the decrease of β and ϵ with height. We use a fixed value $H_0 = 1$ km and consider scenarios with different uplift rates.

The results shown in Fig. 7 reveal a distinct difference not only in mountain height, but also in mountain range asymmetry and spatial gradients in precipitation rate. As expected, mean and peak elevation increase with uplift rate. In strong contrast to scenarios of uniform precipitation, the highest mean and peak elevations are shifted towards the leeward side of the mountain range. The observed asymmetry with a gentle increase in elevation on the windward side and a strong decrease on the leeward side increases with uplift rate. In all scenarios, the highest rates of effective precipitation occur at the windward side of the mountain range, but these spatial gradients in precipitation rate increase distinctly with uplift rate. At an uplift rate of 1.5 km Myr^{-1}, the average effective precipitation decreases by a factor of about five from the windward to the leeward mountain front (Fig. 7i). The principal drainage divide is shifted towards the leeward side with increasing precipitation gradient and uplift rates, but to a much lesser extent than the distribution of mountain heights would suggest.

As illustrated in Fig. 8, the relationship between uplift rate and mountain height becomes nonlinear in contrast to simple scenarios assuming a uniform precipitation rate. At small uplift rates, the behavior is dominated by the increase in precipitation with increasing topography, which results in higher erosion rates. As a consequence, the topography still increases with uplift rate, but the increase is weaker than linear. For the scenario considered here, this holds for uplift rates of up to about 0.5 km Myr^{-1}.

The concavity of the relation between uplift rate and topography is lost at higher uplift rates. The limited amount of moisture supplied from the boundary plays a central part here. As a consequence, the mean effective precipitation rate approaches a constant value for large uplift rates. However, even a constant mean precipitation rate does not imply a linear relation between
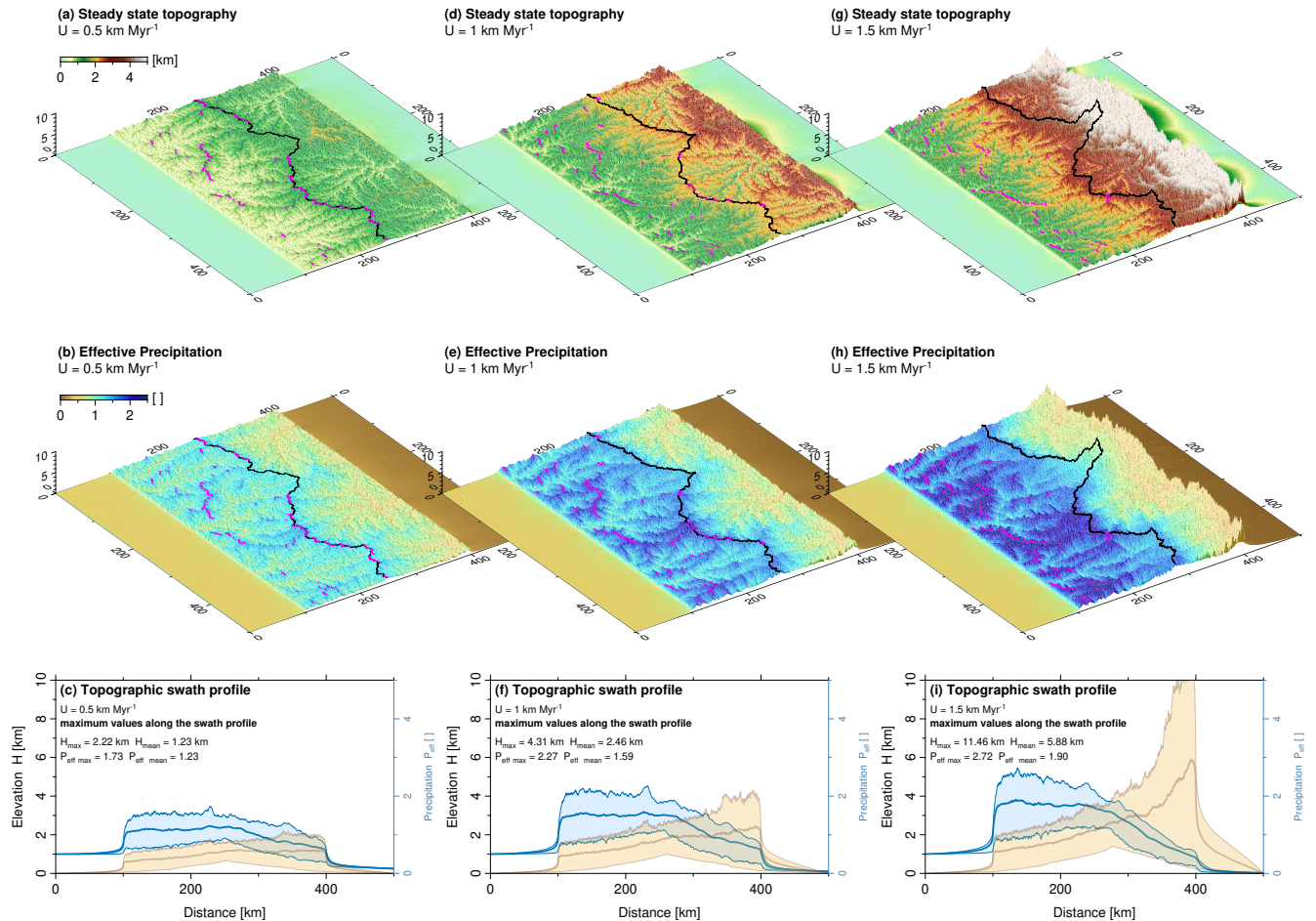
Figure 7. Impact of uplift rate on the precipitation pattern and on mountain geometry for $K = 2.5$ Myr^{-1} and $L_l = 500$ km, $L_c = L_f = 25$ km, $L_d = 5$ km and $\epsilon = 0.5$. (a, d, g) show steady-state mountain topographies representing uplift rates of 0.5 km Myr^{-1}, 1.0 km Myr^{-1} and 1.5 km Myr^{-1}. The black solid line indicates the main drainage divide. Magenta dots mark the position of maximum precipitation in windward direction. (b, e, h) show the corresponding precipitation patterns and (c, f, i) are south-north trending swath profiles representing topography (brown) and effective precipitation (blue) with average (thick solid line) and extreme values (thin solid lines) taken over the full west-east extent of the model domain.
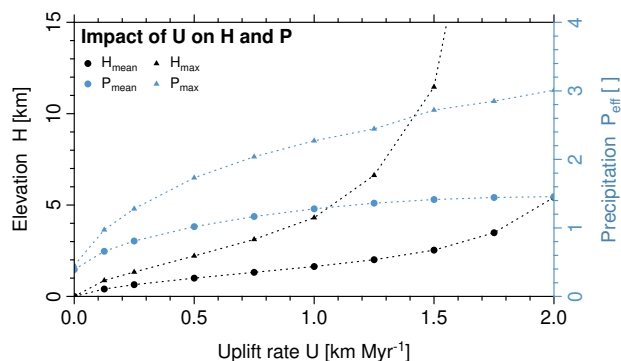
Figure 8. Uplift rate control on precipitation rate and mountain height. Mean and maximum values for precipitation and elevation are computed for the domain of the mountain range only.
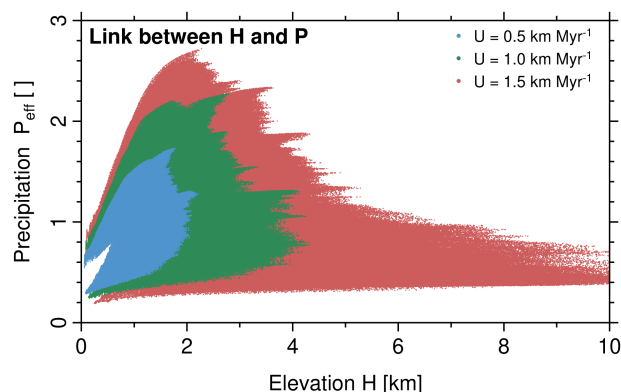
Figure 9. Relationship between surface elevation and precipitation for varying uplift rates (scenarios are shown at Fig. 7).

535   uplift rate and topography since the spatial distribution of the precipitation becomes increasingly inhomogeneous. This effect is recognized in the maximum precipitation rate in Fig. 8, which continuously increases with increasing uplift.

     Figure 9 illustrates the relation between topography and precipitation for the three considered uplift rates. A bimodal distribution is found at low elevations. As shown in Fig. 7(c,f,i), low elevations occur along big valleys close to the boundaries of the mountain range. Since precipitation decreases systematically from the windward side to the leeward side, the low-elevation

540   range splits up into a rather wet windward domain and a rather dry leeward domain. This distinction is, however, lost with increasing surface height since intermediate elevations are distributed over the entire mountain range. This goes along with a rapidly increasing variability in precipitation at given elevation.

     While some decline of the increase in precipitation with elevation is already visible for $U = 0.5\,\mathrm{km\,Myr}^{-1}$, it even turns into an absolute decrease at large elevation. The highest precipitation rates are found at $H \approx 2\,\mathrm{km}$ for $U = 1\,\mathrm{km\,Myr}^{-1}$ as well as

545   for $U = 1.5\,\mathrm{km\,Myr}^{-1}$ and decrease above this elevation. This decrease is not an immediate effect of the height since the model

itself predicts a continuous increase in precipitation with elevation at a given moisture content. As discussed above, it arises from the limited amount of moisture supplied from the windward boundary. So the occurrence of the highest precipitation rates at $H \approx 2$ km is not only related to the parameters of the precipitation model, but also to the properties of the erosion model. As a further consequence, an extreme variation in precipitation occurs at $H \approx 2$ km with high rates at the windward side and

550   very dry regions in the shadow or high mountains where most of the available moisture has already been consumed.

The decrease in precipitation at large elevations results in a strong interaction with landform evolution. Since the erosion rate at a given channel slope decreases then, an equilibrium between uplift and erosion can only be achieved by increasing the channel slopes. Since this also requires increasing heights, a positive feedback occurs. This feedback is visible as a convex relation between uplift rate and elevation in Fig. 8, which means that elevation increases stronger than linearly with uplift rate.

555   This effect is particularly strong in the maximum elevation. It corresponds to the formation of very high peaks close to the leeward boundary of the mountain range (Fig. 7e,i), while the major valleys between these peaks are not particularly high.

While the precipitation pattern explains several properties of the resulting topography, we should keep in mind that the erosion rate depends on the discharge and not on the local precipitation rate. A consequence of this difference is recognized in the leeward foreland in Fig. 7. While the precipitation rate is overall low here, the topography becomes highly variable for

560     $U = 1.5 \, \text{km Myr}^{-1}$.

Huge alluvial fans form behind the highest regions (at $x \approx 200$ km and at $x \approx 400$ km). Their occurrence is related to the low precipitation in the northern foreland. Figure 10(a) reveals that the respective catchments are quite small and completely in the precipitation shadow of the large massifs. This results in a very low discharge and thus in a limited ability to transport the sediment coming from the high mountain region. In equilibrium, the low discharge must be compensated by a high channel

565   slope, which leads to the formation of the huge alluvial fans.

The regions between these fans feature rivers with large catchments which reach deep into the mountain range up to the principal drainage divide. Since a part of the moisture coming from the windward boundary passes the principal drainage divide, parts of these catchments are exposed to high precipitation. As a consequence, the respective rivers feature rather high discharges, although the precipitation rate in the leeward foreland is overall low. Therefore, these rivers are able to carry the

570   sediment coming from the mountain region without forming large alluvial fans.

Figure 10(c) shows that the windward foreland also features rivers with strongly different ratios of discharge and catchment size. While the reason for this variation is basically the same as in the leeward foreland, the variation is less pronounced here since the windward foreland region is exposed to a higher precipitation than the leeward foreland. Concerning the resulting topography, however, the main difference between the two foreland regions consists in the presence of low-discharge rivers

575   bringing sediments from the mountain range to the leeward foreland. In the windward foreland, rivers with low discharge to catchment-size ratio typically have their source in the foreland itself and thus carry only a small amount of sediment. Therefore, the windward foreland features no big alluvial fans.

As shown in Fig. 10(d), the difference in the discharge characteristics between the leeward side and the windward side is not restricted to the foreland regions. The discharge at any given catchment size $A \geq 10 \, \text{km}^2$ varies by less than a factor of 2 at the

580   windward side, while the variation at the leeward side is higher.
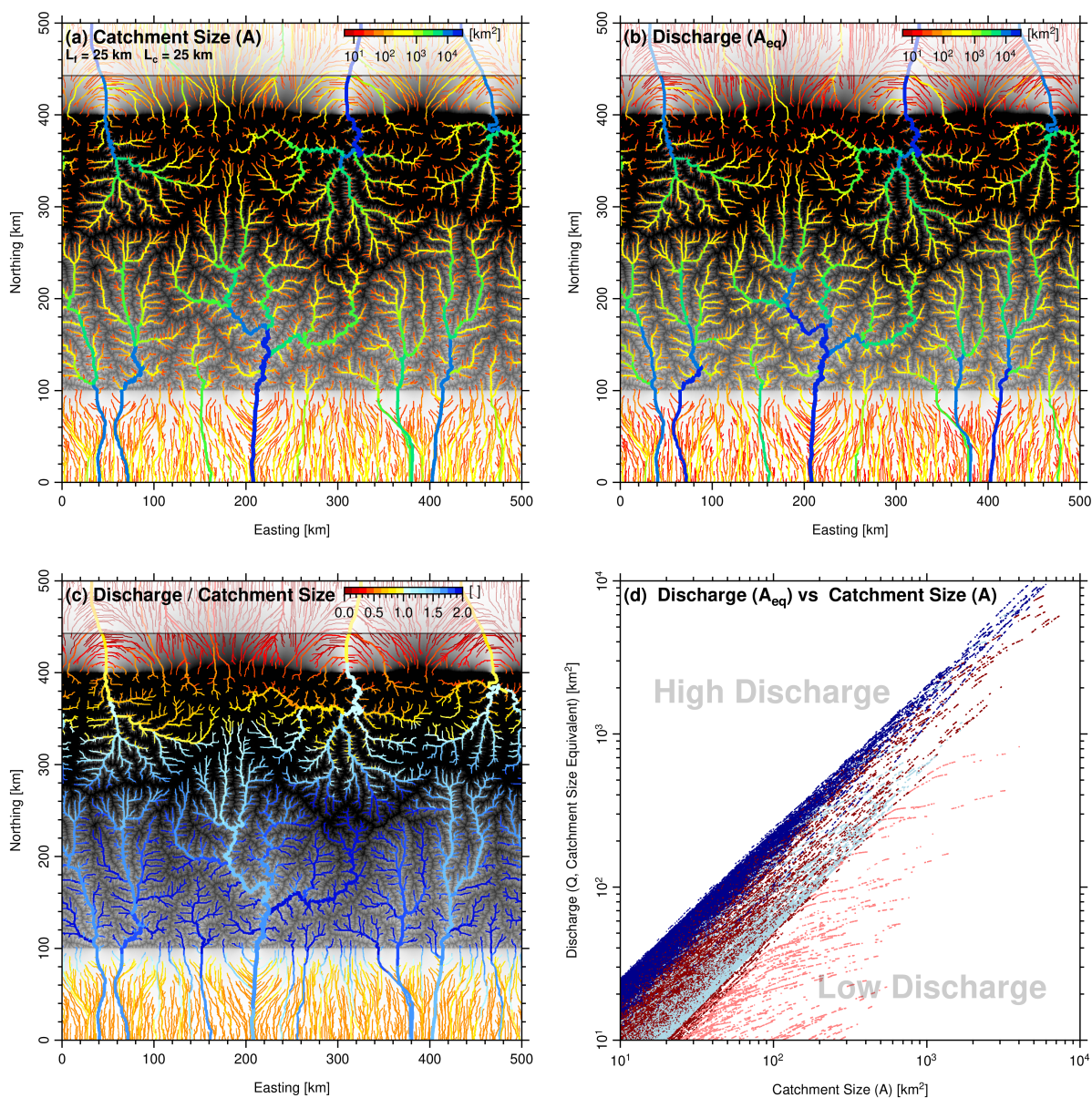
Figure 10. Spatial distribution of precipitation and discharge for $U = 1.5$ km Myr^{-1}, $K = 2.5$ Myr^{-1}, $L_l = 500$ km, $L_c = L_f = 25$ km, $L_d = 5$ km, and $\epsilon = 0.5$. Topography and precipitation pattern of this scenario is shown on Fig. 7 (right column). Channels color-coded for (a) contributing drainage area and (b) river discharge as catchment-size equivalent A_{eq}. (c) ratio of discharge A_{eq} and catchment size A. All channels with a catchment size $A \geq 25$ km^2 are considered. The black solid line follows the main drainage divide. (d) Relationship between catchment size and discharge at the windward (blue dots) and the leeward (red dots) side of the mountain range. Dark colors represent the mountain range and light colors the forelands.

Following individual rivers downstream, the change in the discharge characteristics is opposite in both domains. It is recognized in Fig. 10(c) that rivers originating close to the principle drainage divide start with similar discharge to catchment-size ratios at both sides. However, tributaries at the windward side are rather exposed to higher precipitation, so that the discharge to catchment-size typically increases downstream at the windward side until the rivers reach the foreland. In turn, tributaries

585 at the leeward side are typically quite dry and thus cause a downstream decrease in the discharge to catchment-size ratio. As a consequence, equilibrium profiles of tributaries at the leeward side are rather steep compared to the main rivers, which corresponds to a deeper incision of the large river valleys than at the windward side.

8   Conclusions

This study presents a new model for orographic precipitation for use in large-scale landform evolution models such as the

590 SPIM or the shared stream-power model. The goal was to arrive at a model that goes clearly beyond the simplest concepts such as predicting the precipiation rate directly from surface height or local slope, but to stay at a level of complexity consistent with simple landform evolution models. In particular, the numerical complexity should not be much higher than that of the respective landform evolution models.

We arrived at a model with two moisture components, which are interpreted as vapor and cloud water. In contrast to previous

595 models used in this context, a two-way conversion between both components was assumed without considering a thermodynamic equilibrium explicitly. While this concept, where an equilibrium develops dynamically, seems to be more complicated first, it helps to navigate around some problems and requires little further assumptions.

As a key property, our model captures a decrease in precipitation with increasing distance from the ocean (or any other source of moisture). This decrease is very slow over large continental areas with little topography, but becomes faster if orographic

600 precipitation at large mountain ranges consumes a considerable part of the available moisture. While precipitation overall increases with elevation in the model, it may decrease again at high elevations due to the limited amount of moisture. As a second important property, precipitation responds to changes in topography not instantaneously, but with a finite length scale. Therefore, the model is not sensitive to the small-scale roughness of the topography and can be operated without any additional smoothing.

605 The length scale of the decrease in precipitation due to the limited amount of water and the length scale of the response to changes in topography can be computed from the velocity of transport in the atmosphere and the time scales of the conversion between vapor and cloud water and of the fallout of precipitation. The model structure proposed here is in principle the minimum model that is able to reproduce a long-range transport and a response to changes in topography with a finite length scale.

610 The model also includes dispersion of the moisture fluxes in direction perpendicular to the main transport direction. This component of the model is particularly useful in combination with two-dimensional landform evolution models since precipitation shadows of infinite length would occur behind individual peaks otherwise. Numerically, the dispersion is the most expensive part of the model. However, it can be implemented as a series of one-dimensional diffusion problems as long as

the main direction of transport follows one of the principal coordinate axes. The numerical complexity is still linear then,
which means that the computing effort increases only linearly with the total number of nodes of the grid. Since contemporary,
fully implicit numerical schemes for the respective erosion models are also of linear complexity, this property is essential for
preserving the high numerical efficiency of these models.

The model can easily be extended by a simple model of evapotranspiration where a height-dependent fraction of the precipitation is returned to the atmosphere. While this extension increases the length scale of long-range transport further, it does not
change the properties of the model fundamentally.

Even the simple examples presented in this study show the remarkable impact of continentality and orographic precipitation
on mountain range geometry and the coevolution of topography and precipitation pattern. Future studies can use this numerically efficient approach to address a wide range of research questions in the field of landscape evolution, where the assumption
of uniform precipitation is too simple to explain landscape metrics and topographic pattern.

Code and data availability. The open-source landform evolution model OpenLEM is freely available at http://hergarten.at/openlem. An
additional package that contains the extension presented in this paper and further codes and results of the simulations is available at http://hergarten.at/openlem/gmd-2021-179.zip (preliminary location during the review phase). The authors are happy to assist interested readers
in reproducing the results and performing subsequent research.

Video supplement. The video supplement includes the respective time-dependent simulations of Sect. 7.2.

Author contributions. S.H. developed the theory and the main parts of the codes. J.R. performed the simulations and analyzed the data. Both
authors wrote the paper.

Competing interests. The authors declare that they have no conflict of interest.

Acknowledgements. The numerical simulations were performed on the Doppler HPC-facility of the university of Salzburg. All figures were
generated with the Generic Mapping Tools (Wessel et al., 2019).

635 **References**

Bonnet, S.: Shrinking and splitting of drainage basins in orogenic landscapes from the migration of the main drainage divide, Nat. Geosci.,
2, 766–771, https://doi.org/10.1038/ngeo666, 2009.

Braun, J. and Willett, S. D.: A very efficient O(n), implicit and parallel method to solve the stream power equation governing fluvial incision
and landscape evolution, Geomorphology, 180–181, 170–179, https://doi.org/10.1016/j.geomorph.2012.10.008, 2013.

640 Chen, S.-A., Michaelides, K., Grieve, S. W. D., and Singer, M. B.: Aridity is expressed in river topography globally, Nature, 573, 573–577,
https://doi.org/10.1038/s41586-019-1558-8, 2019.

Davy, P. and Lague, D.: Fluvial erosion/transport equation of landscape evolution models revisited, J. Geophys. Res. Earth Surf., 114,
F03 007, https://doi.org/10.1029/2008JF001146, 2009.

Deal, E. and Prasicek, G.: The sliding ice incision model: A new approach to understanding glacial landscape evolution., Geophys. Res.
645 Lett., 48, e2020GL089 263, https://doi.org/10.1029/2020GL089263, 2021.

Ellis, M. A., Densmore, A. L., and Anderson, R. S.: Development of mountainous topography in the Basin Ranges, USA, Basin Res., 11,
21–41, https://doi.org/10.1111/j.1365-2117.1999.00087.x, 1999.

Garcia-Castellanos, D.: The role of climate during high plateau formation. Insights from numerical experiments, Earth Planet. Sci. Lett., 257,
372–390, https://doi.org/10.1016/j.epsl.2007.02.039, 2007.

650 Garcia-Castellanos, D. and Jiménez-Munt, I.: Topographic evolution and climate aridification during continental collision: Insights from
computer simulations, PLoS ONE, 10, e0132 252, https://doi.org/10.1371/journal.pone.0132252, 2015.

Goren, L., Willett, S. D., Herman, F., and Braun, J.: Coupled numerical–analytical approach to landscape evolution modeling, Earth Surf.
Process. Landforms, 39, 522–545, https://doi.org/10.1002/esp.3514, 2014.

Guerit, L., Yuan, X. P., Carretier, S., Bonnet, S., Rohais, S., Braun, J., and Rouby, D.: Fluvial landscape evolution controlled by the sediment
655 deposition coefficient: Estimation from experimental and natural landscapes, Geology, 47, 853–856, https://doi.org/10.1130/G46356.1,
2019.

Hergarten, S.: Transport-limited fluvial erosion – simple formulation and efficient numerical treatment, Earth Surf. Dynam., 8, 841–854,
https://doi.org/10.5194/esurf-8-841-2020, 2020.

Hergarten, S.: A stream-power law for glacial erosion and its implementation in large-scale landform-evolution models, Earth Surf. Dynam.
660 Discuss. (preprint), in review, n/a, https://doi.org/10.5194/esurf-2021-1, 2021.

Hergarten, S. and Neugebauer, H. J.: Self-organized critical drainage networks, Phys. Rev. Lett., 86, 2689–2692,
https://doi.org/10.1103/PhysRevLett.86.2689, 2001.

Hergarten, S., Robl, J., and Stüwe, K.: Tectonic geomorphology at small catchment sizes – extensions of the stream-power approach and the
χ method, Earth Surf. Dynam., 4, 1–9, https://doi.org/10.5194/esurf-4-1-2016, 2016.

665 Howard, A. D.: A detachment-limited model for drainage basin evolution, Water Resour. Res., 30, 2261–2285,
https://doi.org/10.1029/94WR00757, 1994.

Kooi, H. and Beaumont, C.: Escarpment evolution on high-elevation rifted margins: insights derived from a surface process model that
combines diffusion, advection and reaction, J. Geophys. Res., 99, 12 191–12 209, 1994.

Menking, J. A., Han, J., M.Gasparini, N., and Johnson, J. P.: The effects of precipitation gradients on river profile evolution on the Big Island
670 of Hawai'i, GSA Bull., 125, 594–608, https://doi.org/10.1130/B30625.1, 2013.

Molnar, P. and England, P.: Late Cenozoic uplift of mountain ranges and global climate change: chicken or egg?, Nature, 346, 29–34, 1990.

Robl, J., Hergarten, S., and Prasicek, G.: The topographic state of fluvially conditioned mountain ranges, Earth Sci. Rev., 168, 290–317, https://doi.org/10.1016/j.earscirev.2017.03.007, 2017.

Roe, G. H.: Orographic precipitation and the relief of mountain ranges, Annu. Rev. Earth Planet. Sci., 33, 645–671, https://doi.org/10.1146/annurev.earth.33.092203.122541, 2005.

Roe, G. H., Montgomery, D. R., and Hallet, B.: Orographic precipitation and the relief of mountain ranges, J. Geophys. Res. Solid Earth, 108, 2315, https://doi.org/10.1029/2001JB001521, 2003.

Salles, T.: Badlands: A parallel basin and landscape dynamics model, SoftwareX, 5, 195–202, https://doi.org/10.1016/j.softx.2016.08.005, 2016.

Smith, R. B. and Barstad, I.: A linear theory of orographic precipitation, J. Atmos. Sci., 61, 1377–1391, https://doi.org/10.1175/1520-0469(2004)061<1377:ALTOOP>2.0.CO;2, 2004.

Stock, J. and Dietrich, W. E.: Valley incision by debris flows: Evidence of a topographic signature, Water Resour. Res., 39, 1089, https://doi.org/10.1029/2001WR001057, 2003.

Turowski, J. M.: Semi-alluvial channels and sediment-flux-driven bedrock erosion, in: Gravel-Bed Rivers, edited by Church, M., Biron, P., and Roy, A., chap. 29, pp. 399–418, John Wiley & Sons, Ltd, https://doi.org/10.1002/9781119952497.ch29, 2012.

Wessel, P., Luis, J. F., Uieda, L., Scharroo, R., Wobbe, F., Smith, W. H. F., and Tian, D.: The Generic Mapping Tools version 6, Geochemistry, Geophysics, Geosystems, 20, 5556–5564, https://doi.org/10.1029/2019GC008515, 2019.

Willett, S. D.: Orogeny and orography: The effects of erosion on the structure of mountain belts, J. Geophys. Res. Solid Earth, 104, 28 957–28 981, https://doi.org/10.1029/1999JB900248, 1999.

Willgoose, G.: Mathematical modeling of whole landscape evolution, Annu. Rev. Earth Planet. Sci., 33, 443–459, https://doi.org/10.1146/annurev.earth.33.092203.122610, 2005.

Wobus, C., Whipple, K. X., Kirby, E., Snyder, N., Johnson, J., Spyropolou, K., Crosby, B., and Sheehan, D.: Tectonics from topography: Procedures, promise, and pitfalls, in: Tectonics, Climate, and Landscape Evolution, edited by Willett, S. D., Hovius, N., Brandon, M. T., and Fisher, D. M., vol. 398 of *GSA Special Papers*, pp. 55–74, Geological Society of America, Boulder, Washington, D.C., https://doi.org/10.1130/2006.2398(04), 2006.

Yanites, B. J. and Ehlers, T. A.: Global climate and tectonic controls on the denudation of glaciated mountains, Earth Planet. Sci. Lett., 325–326, 63–75, https://doi.org/10.1016/j.epsl.2012.01.030, 2012.

Yuan, X. P., Braun, J., Guerit, L., Rouby, D., and Cordonnier, G.: A new efficient method to solve the stream power law model taking into account sediment deposition, J. Geophys. Res. Earth Surf., 124, https://doi.org/10.1029/2018JF004867, 2019.